Lithium Leaching–Induced Activation of Spent LFP Composites for Enhanced Water Oxidation with Concurrent Lithium Recovery

Zhihan Xu[a,1], Lun Li[a,1], Jingwen Wei[a,1], Haojing Zhang[a,1], Chao Wu[b], Yilin Dong[a], Shibo Xi[b], Tianze Wu[d], Kangkang Tong[a], Xia Long[a,*], Bora Karasulu[c], Zhichuan J. Xu[d], Ye Zhou[a,*]

a China-UK Low Carbon College, Shanghai Jiao Tong University, Shanghai 200240, P.R. China

b Institute of Sustainability for Chemicals, Energy and Environment (ISCE2), Agency for Science, Technology and Research (A*STAR), 1 Pesek Road, Jurong Island, Singapore 627833, Republic of Singapore

c Department of Chemistry, University of Warwick, Coventry CV4 7AL, U.K.

d School of Materials Science and Engineering, Nanyang Technological University, Singapore 639798, Singapore

[1] These authors contributed equally to this work.

*Corresponding authors.

Email addresses: yezhou_lcc@sjtu.edu.cn (Y. Zhou), x.long@sjtu.edu.cn (X. Long)

Supplementary Information

Experiments

Synthesis of s-LFP, s-LFP@NiO, s-FP, s-FP@NiO and s-LFP@NiO-PL

s-LFP: The spent $LiFePO_4$ (s-LFP) powder was obtained from spent lithium-ion batteries. The full batteries were disassembled in a glovebox full of Ar. And the cathode was cleaned with dimethyl carbonate (DMC) to remove the residual electrolyte. The cathode materials were exfoliated from the current collector (Al foil) by soaking the cleaned cathode in hot water (95 °C, 10 seconds). Dried and ground into powder, the derived $LiFePO_4$ was then washed and centrifuged using N-methylpyrrolidone (NMP) three times to clean the binder polyvinylidene

fluoride (PVDF). The precipitate was dried in vacuum oven overnight to obtain the s-LFP powder.

s-LFP@NiO: The s-LFP@NiO was prepared by a solvothermal method consisting of a two-step heating process.[1] s-LFP (60 mg), nickel(II) acetylacetonate ($Ni(acac)_2$, 120 mg) and hexadecylamine (480 mg) were added into mesitylene (16 mL) and sonicated for 20 min to form a well-dispersed suspension. The suspension was then transferred into a 50 mL Teflon hydrothermal reactor. The solvothermal reaction was conducted with constant stirring in an oil bath. Firstly, the reactor was heated to 170 ℃ for 60 min. Subsequently, it was heated to 200 ℃ for 75 min. After the reaction was completed and cooled to room temperature, the suspension was washed and centrifuged using ethanol and water repeatedly for five times. The collected precipitate was dried in a vacuum oven overnight to obtain s-LFP@NiO powder.

s-FP and s-FP@NiO: The s-LFP powder was dispersed by sonification into a $K_3[Fe(CN)_6]$ solution (0.2 M), which acted as an oxidizing agent.[2] The mixture was allowed to stand overnight to realize a complete extraction of Li ions and form $FePO_4$ (s-FP). The resulting powder was collected via centrifugation and washed several times with Deionized water (DI water). Subsequently, the collected precipitate was dried in a vacuum oven overnight to obtain s-FP powder. The s-FP@NiO was prepared identically to s-LFP@NiO, except for replacing s-LFP (60 mg) by s-FP (60 mg) obtained above.

s-LFP@NiO-PL: The as-synthesized s-LFP@NiO powder was dispersed into a $K_3[Fe(CN)_6]$ solution (0.2 M), which acted as an oxidizing agent.[2] The mixture was allowed to stand overnight to achieve complete extraction of Li ions. The resulting s-LFP@NiO-PL (PL stands for pre-leaching of lithium ions) powder was collected via centrifugation and washed several times with DI water. After drying overnight in a vacuum oven, the s-LFP@NiO-PL powder was obtained.

Selective recovery of lithium from the lithium-rich $K_3[Fe(CN)_6]$ suspension

The lithium-rich $K_3[Fe(CN)_6]$ suspension was filtered and the solution was evaporated to one-fifth of its original volume to increase the lithium concentration. The pH value of the solution was then adjusted to 7.5-8.5 by adding NaOH to remove impurities such as iron. After filtering the precipitate, Na_2CO_3 was added to the solution to react with the lithium ions and form the

lithium salt Li_2CO_3. During the precipitation process, the solution was continuously stirred at 300 rpm, maintained at a temperature of 95 °C, and the process lasted for 2 hours. The precipitate was filtered, washed with saturated Li_2CO_3 solution and dried.

Electrochemical measurements

Electrode preparation: the catalyst powders were mixed with carbon (mass ratio = 4:1) and then dispersed into a mixture solution containing deionized water, isopropyl alcohol and Nafion (5%) in a volume ratio 3:1:0.2 to obtain a homogeneous ink (381 μg_{cat} mL^{-1}). The resulting catalyst ink was then drop-casted onto the glass carbon electrode (GCE) and allowed to air dry. The mass loading of the catalysts (excluding carbon) was 255 μg cm^{-2}. All the OER measurements, unless explicitly stated otherwise, were implemented on Biologic-SP150 with catalyst on GCE as working electrode, Pt electrode as counter electrode, and Hg/HgO electrode as reference electrode in 1.0 M KOH electrolyte (Fe impurity 281 ppb, measured by ICP-OES). To avoid the potential contamination from glass, all electrochemical tests were conducted using a polypropylene cell, and an alkaline-resistant Hg/HgO reference electrode was used. CV was utilized to obtain the OER polarization curves at a scan rate of 10 mV s^{-1}. Electrochemical impedance spectroscopy (EIS) was operated at 0.65 V vs. Hg/HgO from 100 kHz to 50 mHz. Double layer capacitance (C_{dl}) was obtained by CV within a scan range of -0.05-0.05 V vs. Hg/HgO. Electrochemical surface area (ECSA) of the electrocatalyst was derived from the obtained C_{dl} divided by specific capacitance (C_s) assumed as 40 μF·cm^{-2}. Stability tests show in Figure S15 was conducted at 10 mA cm^{-2}, and all samples were prepared on GCE using the same ink formulation described above. For the durability tests in Figure 2b (in the manuscript), the chronoamperometry (CA) was applied at 250 mA cm^{-2}. The working electrode was prepared by dispersing the catalyst powder (2 mg) in ethanol (440 μL) . To form the catalyst ink, 4 wt% PTFE (440 μL) suspension was gradually added, and the mixture was sonicated for 2 hours. The resulting catalyst ink was then coated onto Ni foam and air-dried, with a catalyst mass loading of 2 mg·cm^{-2}. All potential measurements, unless explicitly stated otherwise, are converted to the RHE scale.

Anion-exchange membrane water electrolyzer (AEMWE) assembly:

An AEM electrolyzer was assembled with Pt/C as the cathode, and with either RuO_2 or s-LFP@NiO as the anode.

Electrodes were prepared by the drop-casting method. Specifically, 10 mg of the powder was dispersed in a mixture of 400 μL ethanol and 100 μL Nafion to form the ink, followed by ultrasonication for 60 min. The resulting ink was then drop-cast onto nickel foam at a loading mass of 2 mg/cm^2. The geometric area of the electrolytic cell was 1 cm^2 (1 cm×1 cm). 1 M KOH was used as the electrolyte and the flow rate was 5 mL min^{-1}. The electrolysis temperature is 25℃. The model of the anion exchange membrane is fumasep faa-pk-130.

Fabrication of the Raney Nickel/Ni Foam electrode

Nickel foam electrodes (NFE) with 75 pores per inch (PPI) were selected as the substrate. Raney nickel electrodes were fabricated by coating Raney nickel, an alloy of nickel and aluminum, onto the NFE using the atmospheric plasma spraying method to achieve a mass loading of 24 mg cm^{-2}, with a nickel mass fraction of 50%. After coating, the aluminum in the Raney nickel was removed by soaking the electrodes in 1 M KOH solution, resulting in a dual-pore structure. This structure comprises micropores on the Raney nickel surface, formed by the dissolution of aluminum, and macropores in the NFE substrate.

Characterization

X-ray diffraction (XRD) analysis was conducted using a D8 ADVANCE Da Vinci diffractometer (Cu Kα, λ=0.154 nm) at a scan rate of 5.0° min^{-1} over a 2θ range from 10 to 90°. Scanning electron microscopy (SEM) utilizing the Sigma 500 model, equipped with energy-dispersive X-ray spectroscopy (EDX), was employed to examine the morphology and elemental composition of the samples. Transmission Electron Microscopy (TEM) and High-resolution Transmission Electron Microscopy (HRTEM) using the Talos F200X G2 was employed to observe the morphology and lattice fringes. Four Silicon Drift Detector's (SDD) are integrated to realize sensitive EDS detection. X-ray photoelectron spectroscopy (XPS) data was collected using the K-alpha light source at 1486.6 eV. To ensure mass loading within the XPS and XRD

detectable limits, multiple samples were prepared by drop-casting ink onto 1*1 cm^2 carbon paper (CP) to obtain a higher mass loading of 500 $\mu g \cdot cm^{-2}$.

Computational details

All of the calculations are performed in the framework of the spin-polarized density functional theory with the projector augmented plane-wave method, as implemented in the Vienna ab initio simulation package (VASP)[3, 4]. The generalized gradient approximation (GGA) proposed by Perdew, Burke, and Ernzerhof (PBE) is selected for the exchange-correlation potential[5, 6]. The long-range van der Waals interaction is described by the DFT-D3 approach[7]. The cut-off energy for plane wave is set to 500 eV. The energy criterion is set to 10^{-4} eV in iterative solution of the Kohn-Sham equation. All the structures are relaxed until the residual forces on the atoms have declined to less than 0.05 eV/Å. Data analysis and visualization are carried out with the help of VASPKIT[8] code and VESTA[9]. To avoid interlaminar interactions, a vacuum spacing of 20 Å is applied perpendicular to the slab.

The diffusion barrier at different adsorption sites were explored by using the Nudge Elastic Band (CI-NEB) method[10]. We use the Bader charge to express the charge transfer quantity.

The defect formation energy E_{form} is expressed as

$$E_{form,v} = E_{defect} - E_{perfect} + \sum E_{vacancy}$$

where E_{defect} and $E_{perfect}$ are the energy with and without the defect. $E_{vacancy}$ are the energy of the vacancy atom, respectively.

EXAFS fitting

EXAFS analysis: Data merging, background subtraction, normalization and fitting of the XANES and EXAFS spectra were performed using Demeter software package. The k3 -weighted Fourier transforms for all the EXAFS data were conducted using a Hanning-shaped window. The S_0^2, used in the fitting for the elements Ni and Fe were extracted from the analysis of the EXAFS of the standard metallic foil. The k-ranges and R-ranges for the fitting of all the Ni K-edge EXAFS data were set as 2.5-11.6 $Å^{-1}$ and 1.0-3.0 Å, respectively. The k-ranges and R-ranges for the fitting of all the Fe K-edge EXAFS data were set as 3-11.5 $Å^{-1}$ and 1.0-2.15 Å,

respectively. We performed EXAFS curve fitting by referencing a tutorial book.[11]

ECSA measurements

The ECSA (cm^2) of the catalyst is calculated by following equation:

$$\text{ECSA} = S_{geo} \times \frac{C_{dl}}{C_s}$$

where C_{dl}(μF cm^{-2}) is the experimentally obtained capacitance, C_s(μF cm^{-2}) is the specific capacitance of an atomically smooth planar surface of material per unit area under identical electrolyte conditions (C_S used here is 40 μF cm^{-2}, as a general value of reported TM-based catalysts), and S_{geo}(cm^2) is the geometric area (0.19625 cm^2) of the glassy-carbon electrode.

Double layer capacitance (C_{dl}) was measured by CV within the potential window of -0.05–0.05 V vs. Hg/HgO where no faradic current was observed for 10 cycles at different scan rates (20, 40, 60, 80, 100 and 120 mV s^{-1}). By linearly fitting the charging current density differences against the corresponding scan rate, the C_{dl} can be estimated by the following equation:

$$C_{dl} = \frac{\Delta j}{v} = \frac{|j_c - j_d|}{v} = b_{slope}$$

Where Δj(mA cm^{-2}) is the differences values between charging current density j_c(mA cm^{-2}) and discharging charging current density j_d(mA cm^{-2}), v(mV s^{-1}) is the scan rate, b_{slope}(μF cm^{-2}) is the derived slope value. The C_{dl} can be estimated to be the linear fit slope result of differences between dis/charge current density under each differenet scan rate.

TOF measurement

Turnover frequency (TOF) is defined as the number of O_2 molecules that per electrocatalyst can convert into a product per time according to the following equation:

$$TOF_{redox} = \frac{j \times S_{geo}}{4 \times F \times n}$$

The as-obtained TOF is denoted as TOF_{redox}(s^{-1}), where j(mA cm^{-2}) represents the measured current density at an overpotential of 300 mV, S_{geo}(cm^2) is the working electrode geometric area, F(C mol^{-1}) is the Faradays constant (96485 C mol^{-1}), and n(mol) is the number of active catalytic sites moles determined by Ni redox peak integration.

The number of active sites (n) is estimated via the following method[12]: n (mol) is estimated by the integration of Ni reduction peak at ~1.3 V vs. RHE (assuming a one-electron process of Ni^{3+}/Ni^{2+} reduction reaction):

$$n_{redox} = \frac{Q_{Ni}}{F} = \frac{A_{Ni}/v}{F}$$

where Q_{Ni}(C) represents the calculated charge for Ni reduction reaction, A_{Ni}(mA·V) is the integration CV area of the Ni reduction peak, v(mV s^{-1}) is the scan rate and F(C mol^{-1}) is the Faraday constant.

Life cycle economic costs and benefits

The net cost of our catalyst consists of the s-LFP cost, process cost, material input cost and the benefit derived from the Li salt produced (Table S3). Equipment costs, water consumption and labor costs were not considered. 270 g of spent LFP cathode powder can be obtained from 1 kg of spent LFP batteries. After the solvothermal process, 350 g of s-LFP@NiO was obtained. About 75% of the iron in the spent LFP is Fe^{2+}, so 339 g of s-LFP@NiO-PL can be obtained after the leaching process. The economic analysis for the production of 1 kg of our catalyst is based on the above discussion.

The price of spent LFP battery is 0.044 ¥/g and the price of spent LFP cathode powder is assumed to be half of that of spent battery (0.022 ¥/g).[13, 14] The material input cost includes prices of $Ni(acac)_2$, oxidants and Na_2CO_3. In the solvothermal process, mesitylene and hexadecylamine can be reused, so their costs have been ignored. Approximately 50% of the $Ni(acac)_2$ was consumed so the remaining half can be reused. In the leaching process, three groups of oxidants were selected for economic analysis ($K_3[Fe(CN)_6]$, $Na_2S_2O_8$, $Fe_2(SO_4)_3$).

The prices of the oxidants were averaged in the calculation. The mass of the oxidants is determined based on the number of electrons transferred. In the precipitation process, the mass of Na_2CO_3 and Li_2CO_3 is in proportion to the lithium ions in the solution. The process cost consists of energy consumption of solvothermal process and lithium recovery process. The detailed energy consumption of the processes is listed in Table S5. The price of electricity is 0.79 ¥/kWh. The price of Raney Ni is 667.4 ¥/kg.[15]

The prices of the chemicals are obtained from different purchasing sources[13, 16-30] (Table S4) in June 2024 and a Monte Carlo simulation was conducted to show the uncertainty of the calculation. Prices from different sources of purchase are assumed to follow a normal distribution, with the average price being the mean μ and the lowest price being the lower 95 percent confidence limit (μ-2σ). For this probabilistic model a random sample is taken to obtain the prices of the different chemicals and from this the total cost is calculated. Repeating this process 5000 times yields a probability density curve for the total cost (Figure S22).

Supplementary Figures and Tables

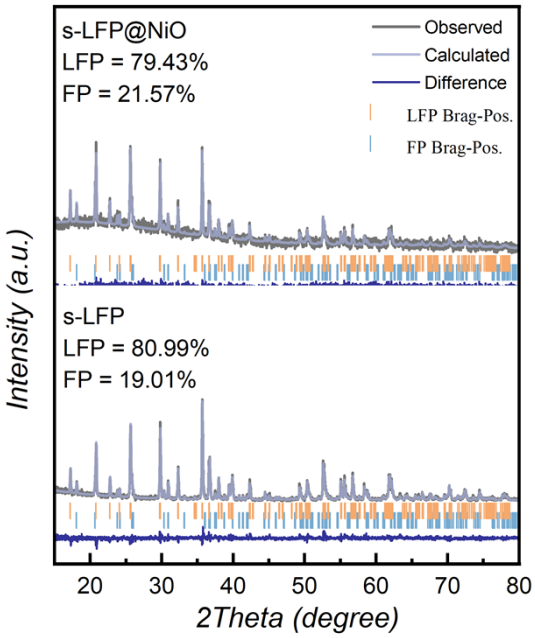

Figure S1. XRD patterns and Rietveld refinement results of s-LFP and s-LFP@NiO.

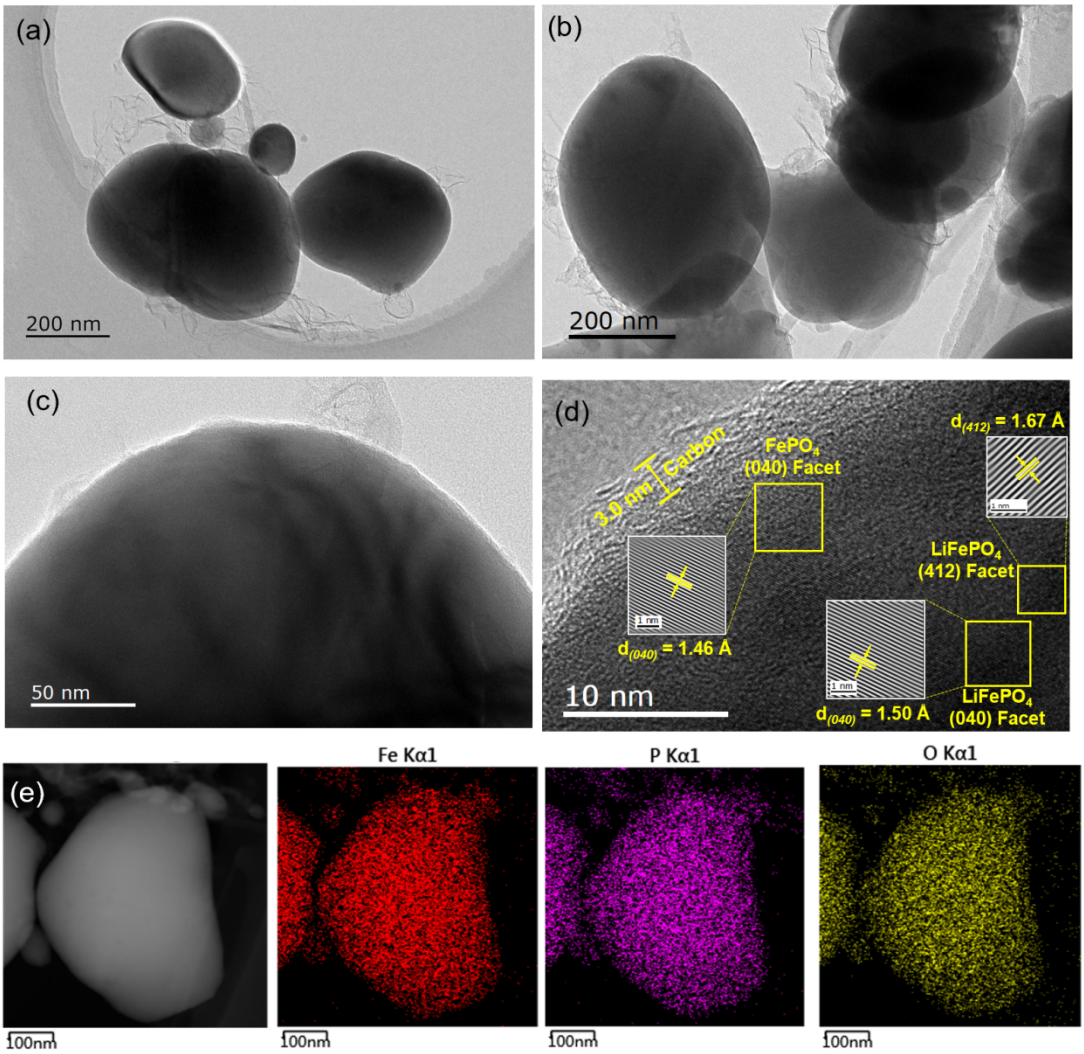

Figure S2. TEM images and elemental mapping of the s-LFP particles.

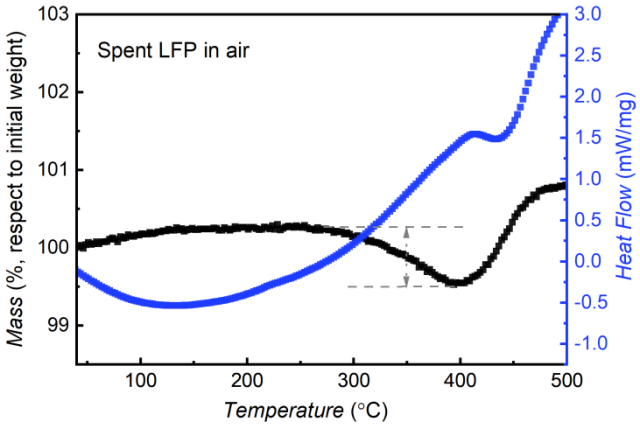

Figure S3. TGA curve of the spent LFP in air; heating rate 10 °C/min.

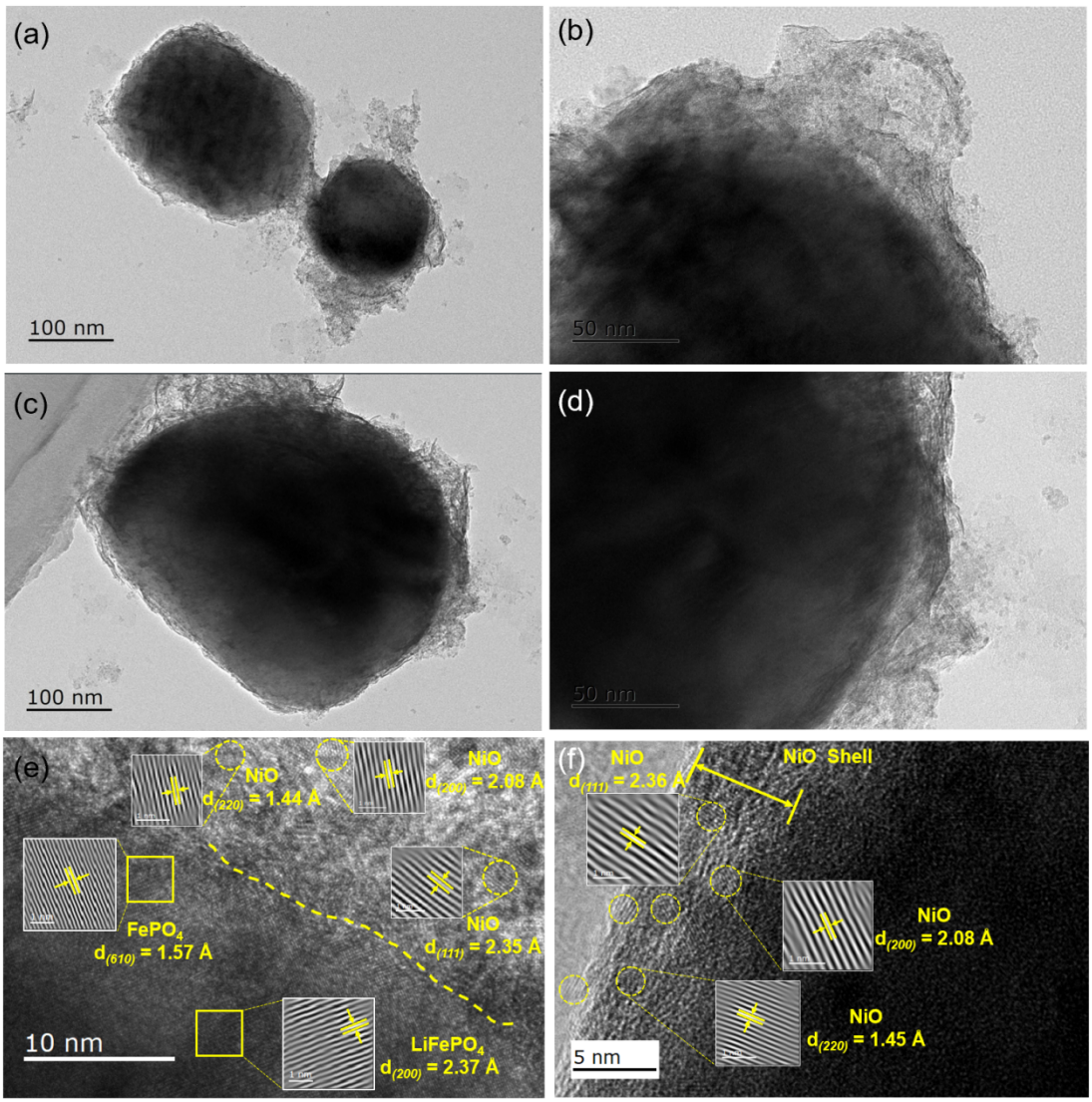

Figure S4. TEM images of the s-LFP@NiO.

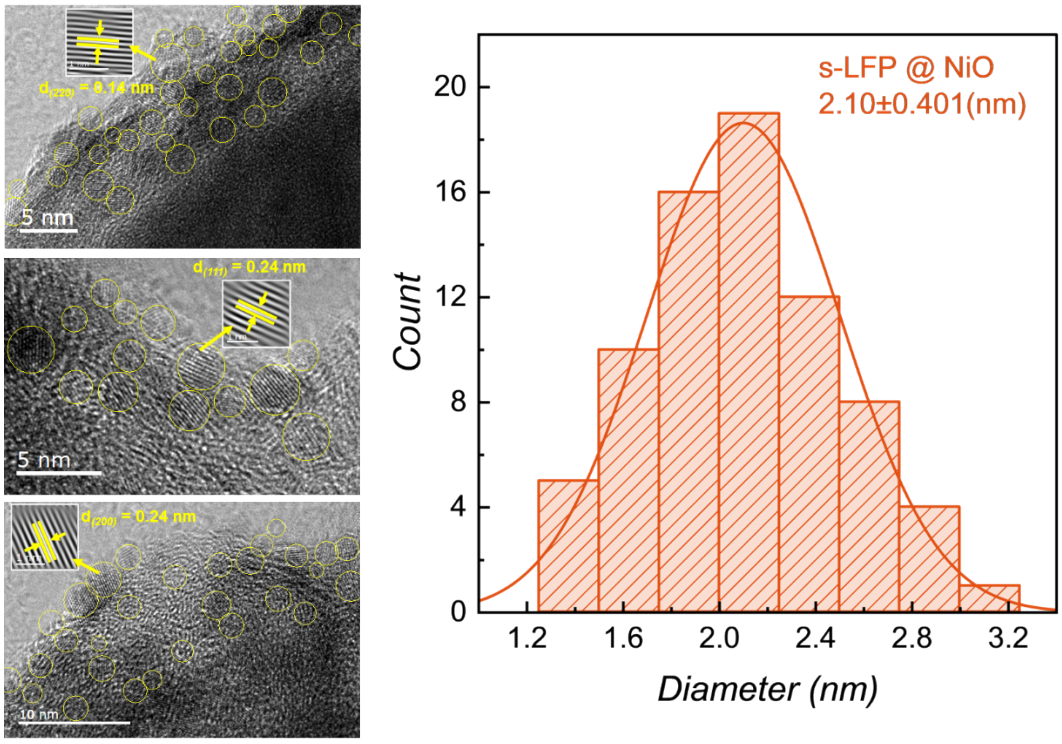

Figure S5. Size distribution of NiO in s-LFP@NiO.

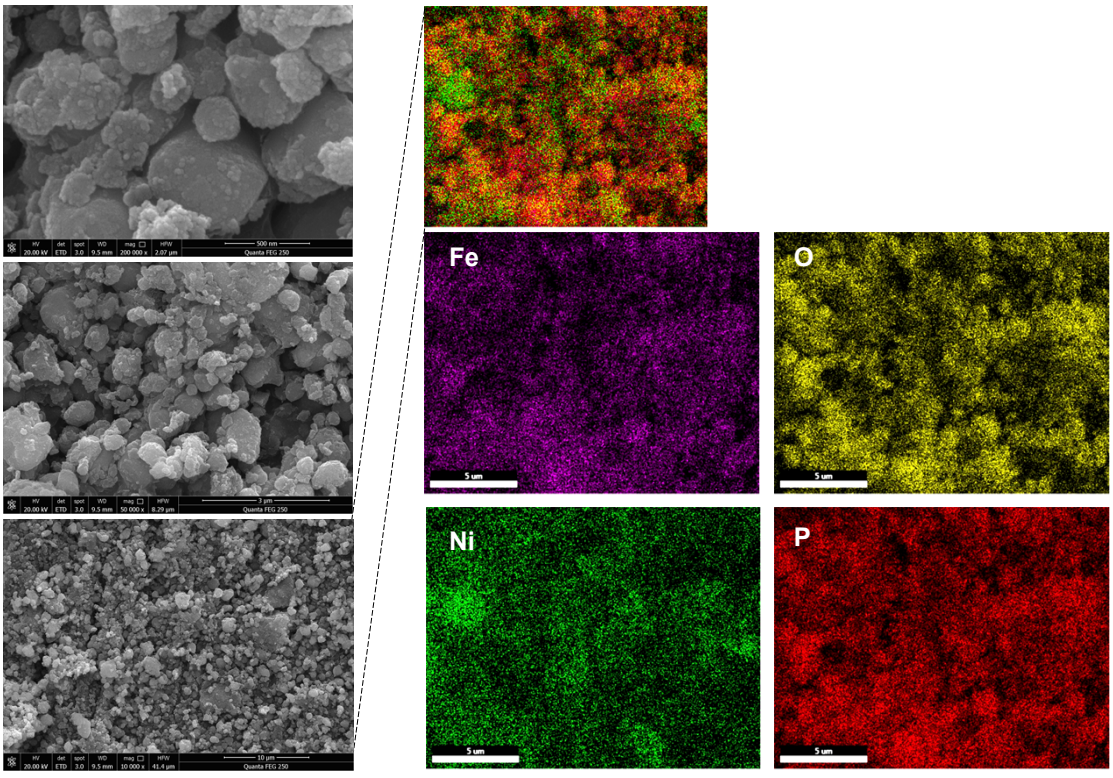

Figure S6. SEM images and elemental mapping of the s-LFP@NiO.

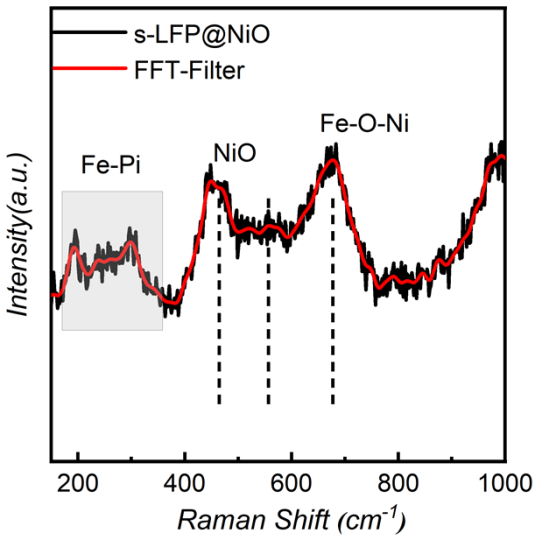

Figure S7. Raman spectra of s-LFP@NiO precatalyst.

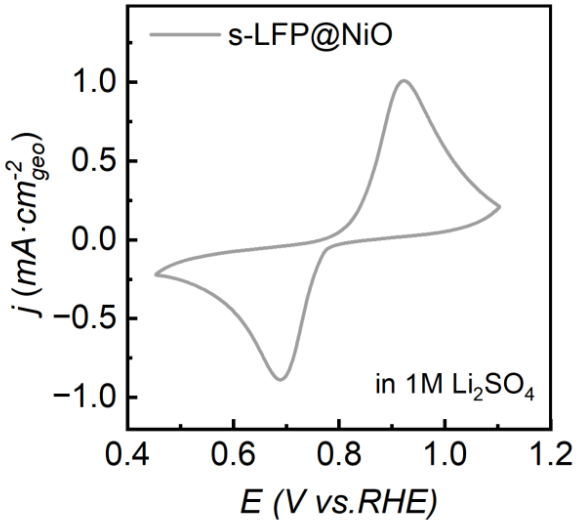

Figure S8. CV scan of the s-LFP@NiO electrode in 1M Li_2SO_4 solution.

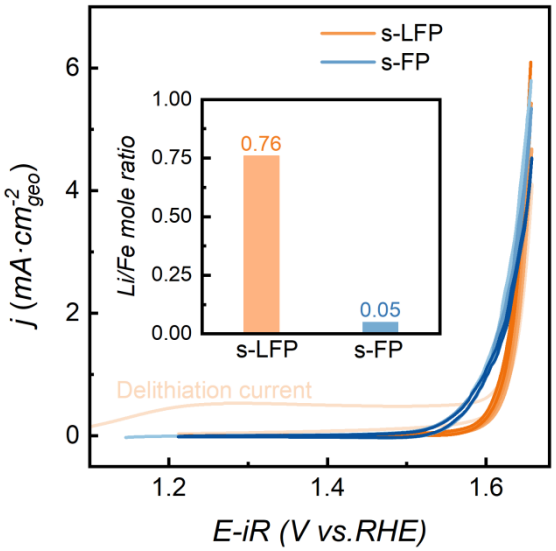

Figure S9. OER CV curves (first 10 cycles) of the s-LFP and s-FP; inset is the Li/Fe ratio determined by ICP-OES.

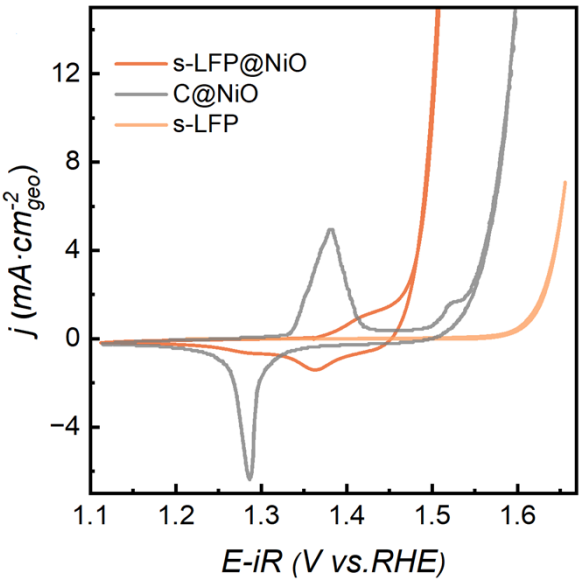

Figure S10. Stabilized OER CV curves of the s-LFP, s-LFP@NiO and the C@NiO electrode

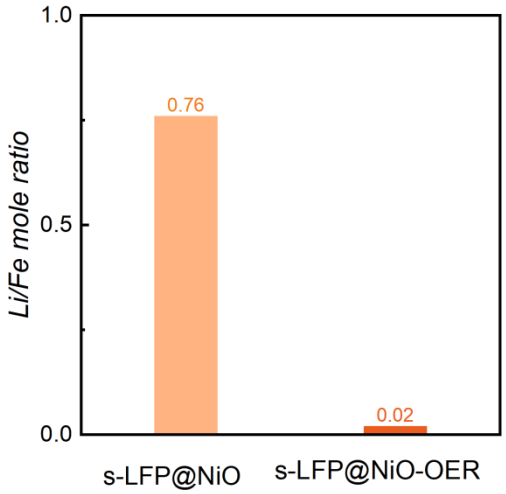

Figure S11. The Li/Fe ratio of the s-LFP@NiO before and after the OER scan, determined by ICP-OES.

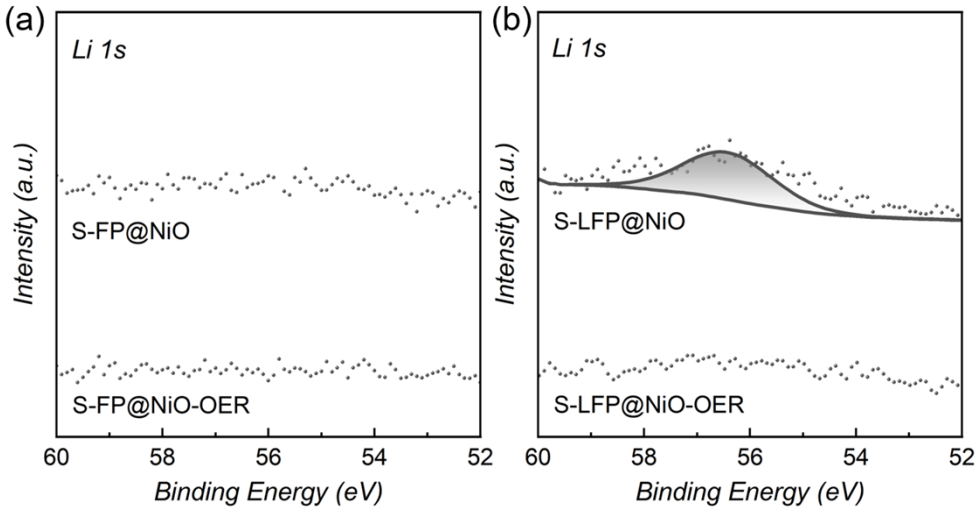

Figure S12. Li 1s XPS spectra of s-FP@NiO and s-LFP@NiO before and after the OER test.

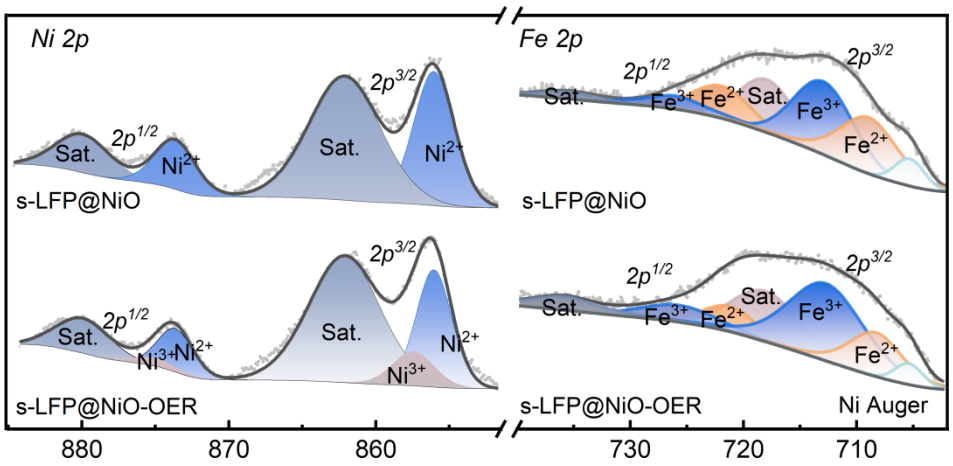

Figure S13. Fe, Ni 2p XPS spectra of s-LFP@NiO before and after the OER test.

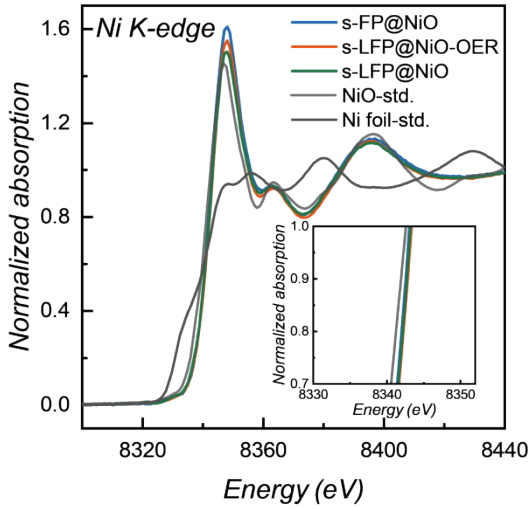

Figure S14. Ni K-edge XANES spectra of s-LFP@NiO, s-LFP@NiO-OER, s-FP@NiO, and the reference NiO and Ni foil. Inset: Enlarged XANES diagram.

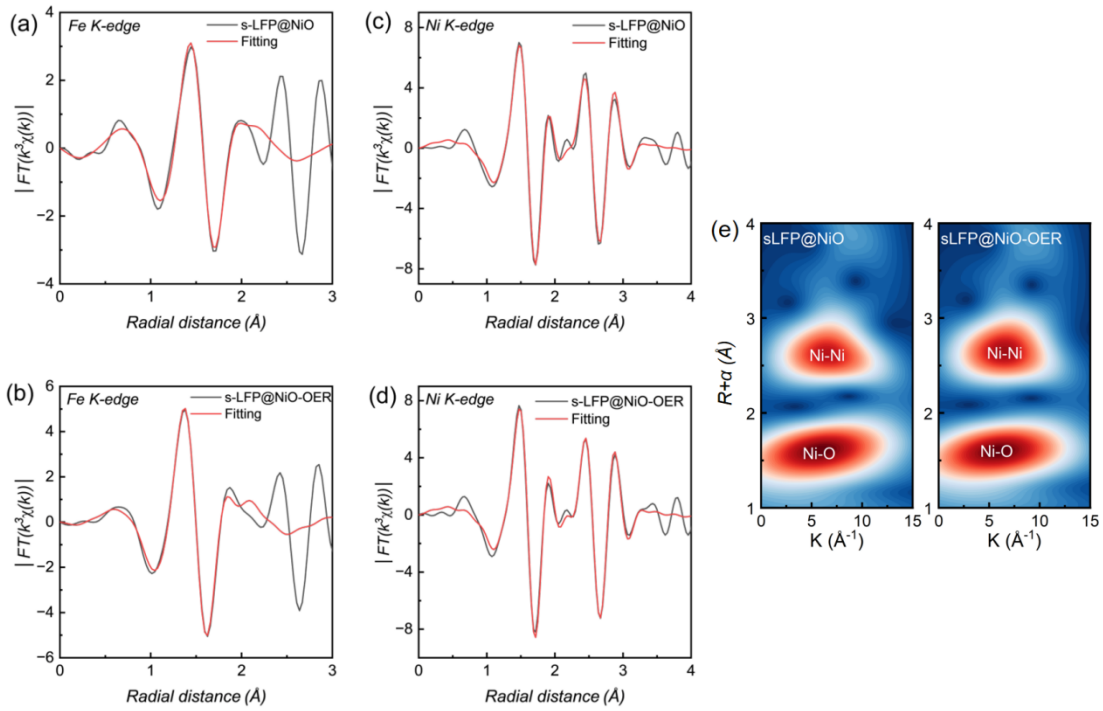

Figure S15. (a-d) Real part of Fourier transforms of EXAFS k3 χ(R) spectra data and fits of s-LFP@NiO and s-LFP@NiO-OER (Fe K-edge and Ni K-edge). (e) Corresponding wavelet transform (WT)-EXAFS contours for s-LFP@NiO and s-LFP@NiO-OER (Ni K-edge).

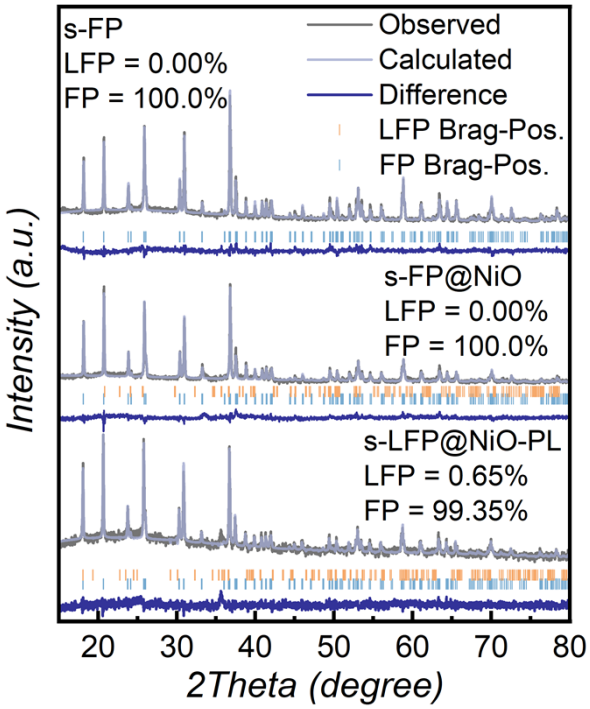

Figure S16. XRD patterns and Rietveld refinement results of s-FP, s-FP@NiO, and s-LFP@NiO-PL.

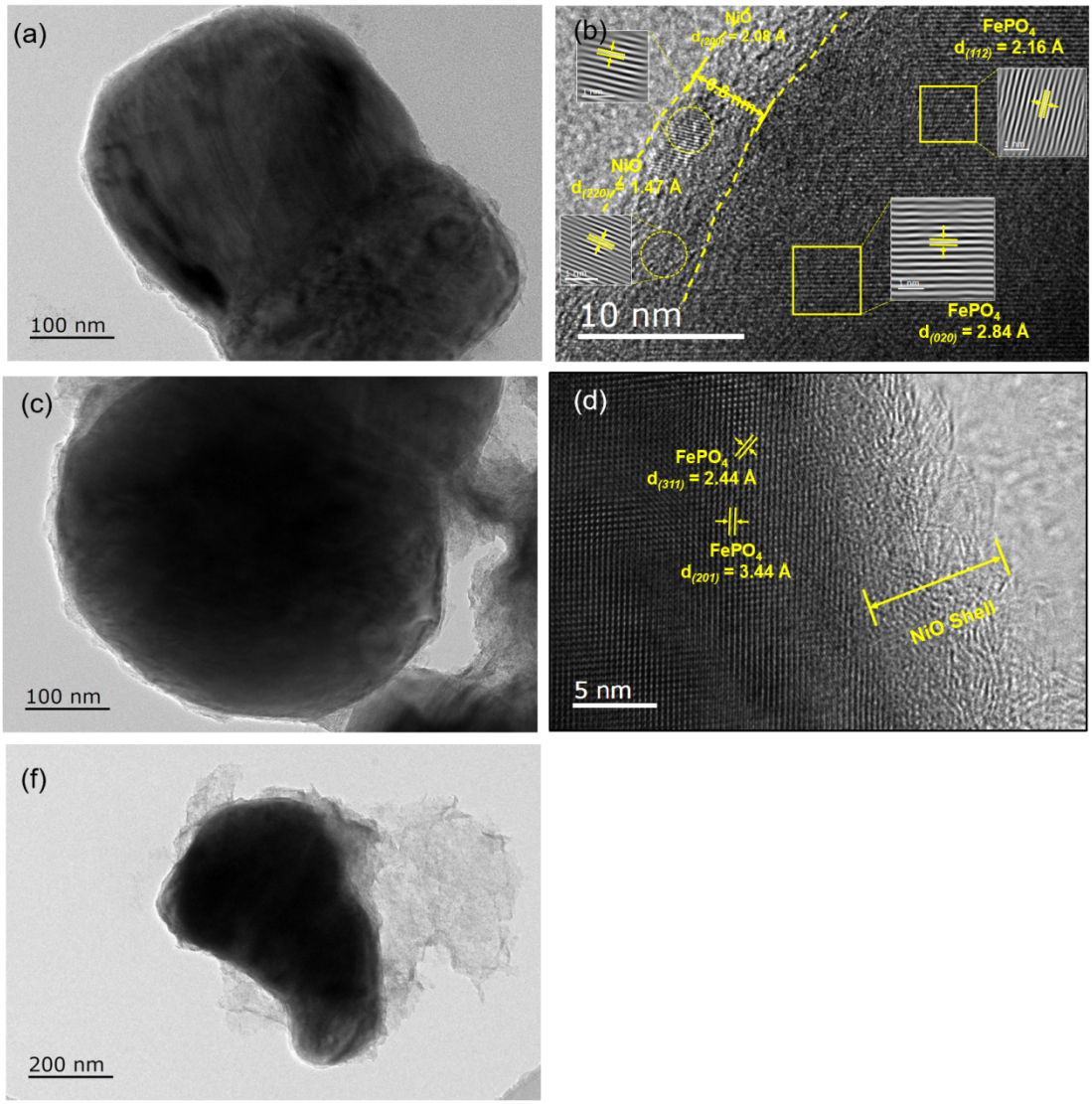

Figure S17. TEM images of the s-FP@NiO.

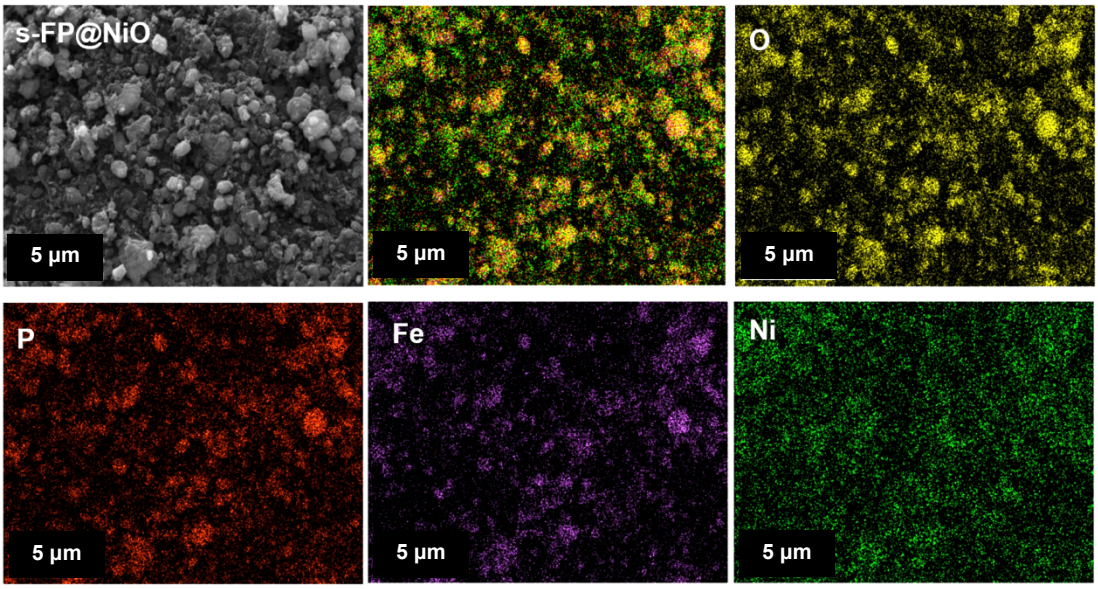

Figure S18. SEM images and elemental mapping of the s-FP@NiO.

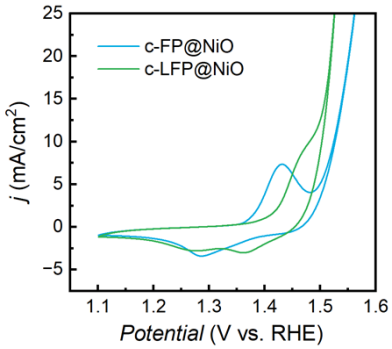

Figure S19. CV curves of c-LFP@NiO and c-FP@NiO in 1 M KOH at a scan rate of 10 mV s^{-1}. To assess the broader applicability of our recycling method to retired LFP batteries with different cycling histories, we applied the identical synthesis and testing protocol to commercial LFP materials (c-LFP) as a representative benchmark. The resulting catalysts, c-FP@NiO and c-LFP@NiO, exhibited OER performance trends consistent with those derived from spent materials: c-FP@NiO showed an overpotential of 297 mV at 10 mA· cm^{-2}, while c-LFP@NiO required only 273 mV.

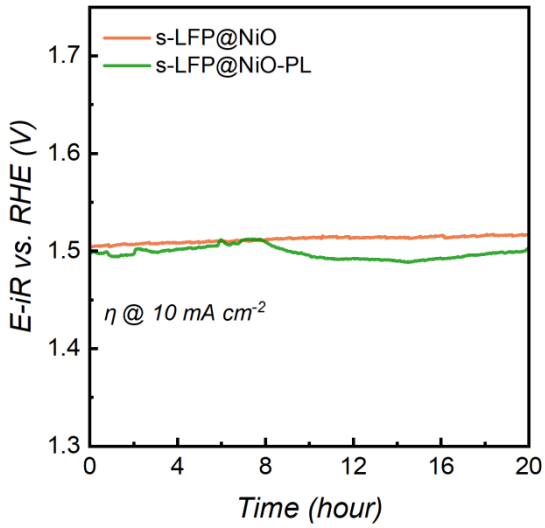

Figure S20. Stability of s-LFP@NiO and s-LFP@NiO-PL catalyst toward OER.

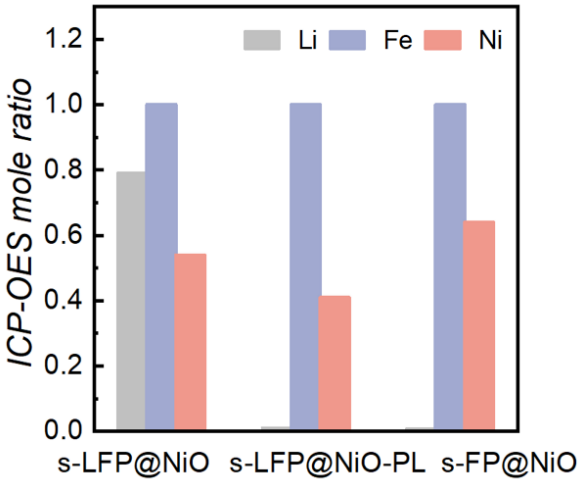

Figure S21. The determined Li/Fe/Ni ratio by ICP-OES test for the s-LFP@NiO, s-LFP@NiO-PL and s-FP@NiO catalysts.

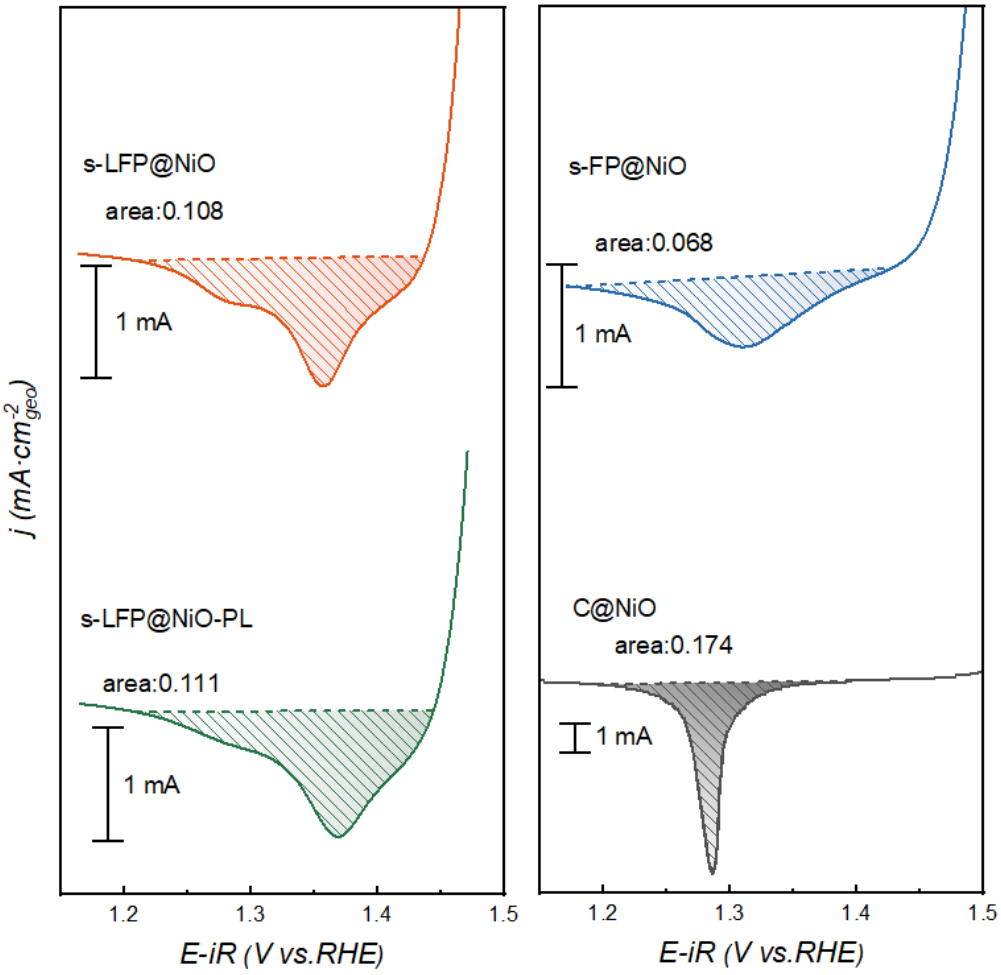

Figure S22. Cathodic charge integration of, s-LFP@NiO, s-LFP@NiO-PL, s-FP@NiO and C@NiO catalyst.

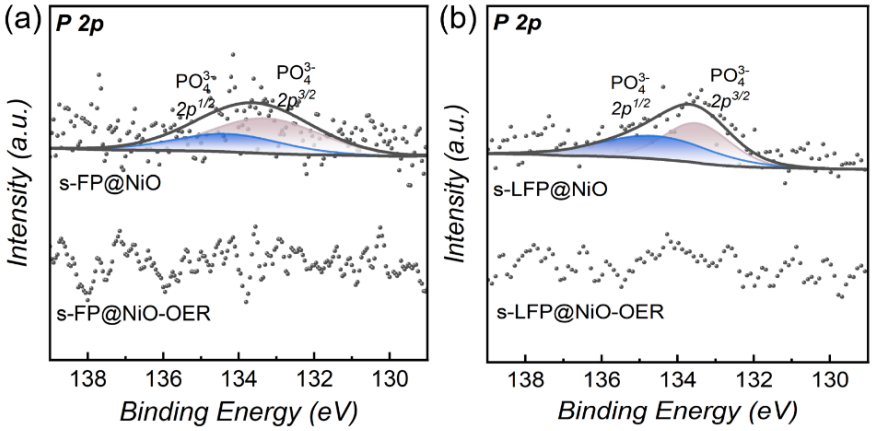

Figure S23. P 2p XPS spectra of s-FP@NiO and s-LFP@NiO before and after the OER test.

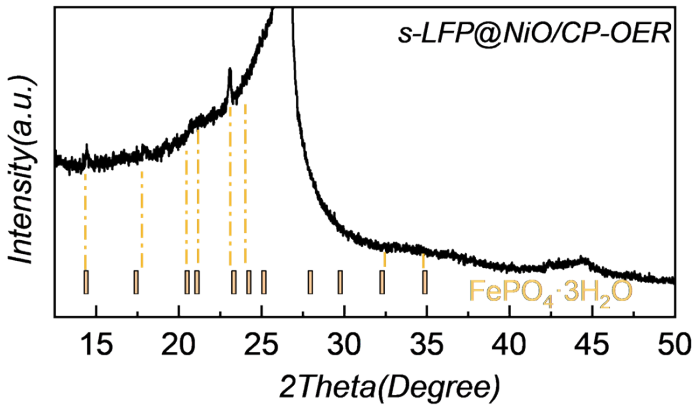

Figure S24. X-ray diffraction pattern of s-LFP@NiO/CP after duration test.

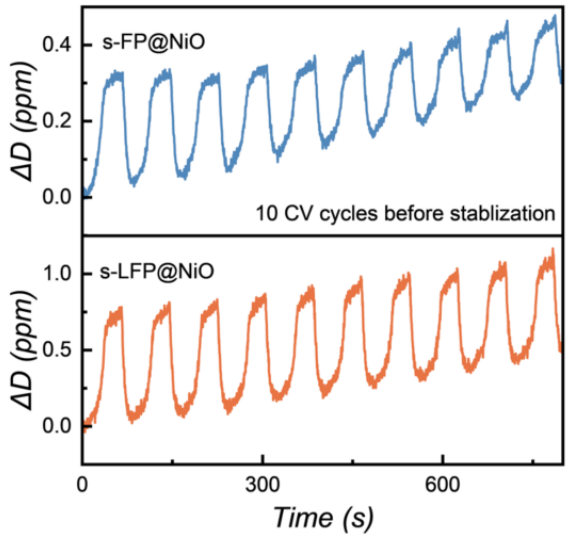

Figure S25. Dissipation (D) vs time during the CV cycles.

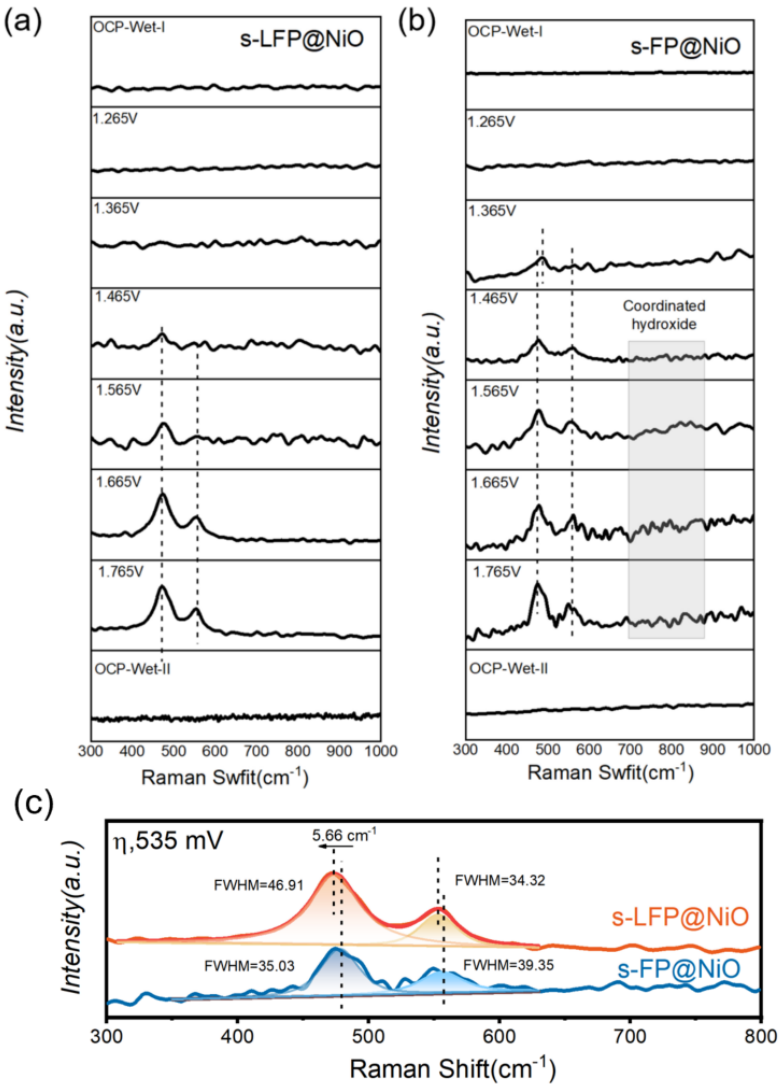

Figure S26. In situ Raman spectra of (a) s-LFP@NiO and (b) s-FP@NiO in 0.1 M KOH. (c) Raman spectral deconvolution of oxyhydroxides for peak positions and half-widths in both samples at η 535mV (1.765 V vs. RHE)

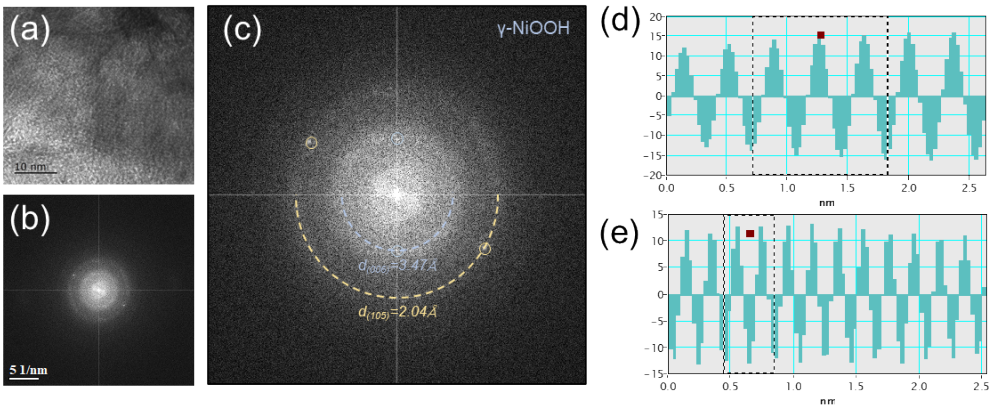

Figure S27. Structural characterization of the s-LFP@NiO-OER catalyst. (a) HR-TEM image of the surface region after OER. (b) Corresponding SAED pattern. (c) Magnified view of the SAED pattern. Measured lattice spacings for the (d) (006) and (e) (105) planes.

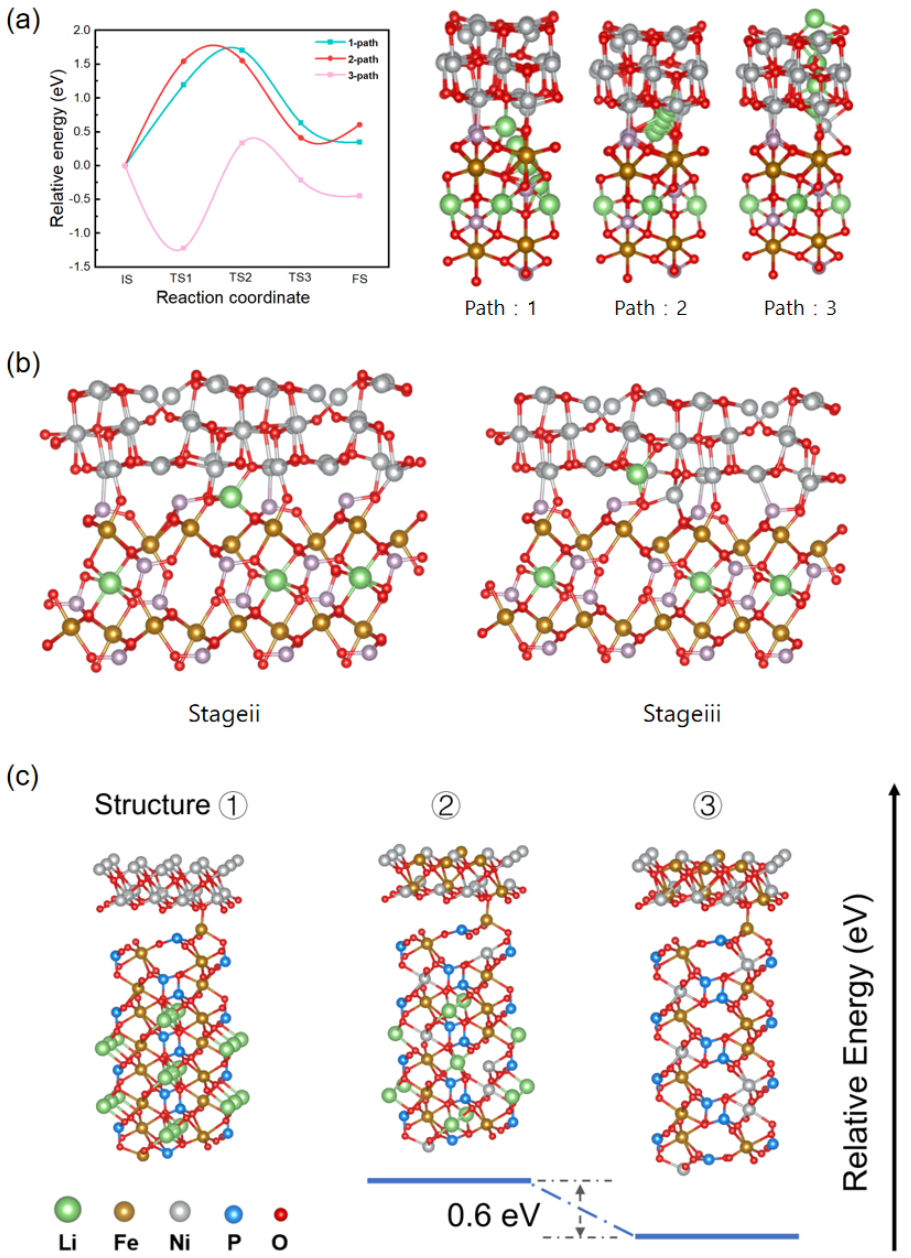

Figure S28. (a) Calculation of the Li migration path using the nudged elastic band (NEB) method. (left) Energy profile and (right) atomic models, for Li^+ extraction via different diffusion channels within the heterojunction. (b)Snapshot configurations at intermediate stage ii and iii from the primary paths.(c) Energy calculations to probe the effect of gradual Li loss on the mixed Ni-Fe surface composition. The structures used for DFT formation energy calculations. Structure 1: $LiFePO_4$-$FePO_4$-NiO(topmost); Structure 2: Li_xMPO_4($x\approx0.5$)-MPO_4-MO(topmost); Structure 3: MPO_4-MO(topmost); M stands for Fe/Ni. The formation energy for structure 2 and structure 3 is 14.62 eV and 14.02 eV, respectively, with respect to structure 1.

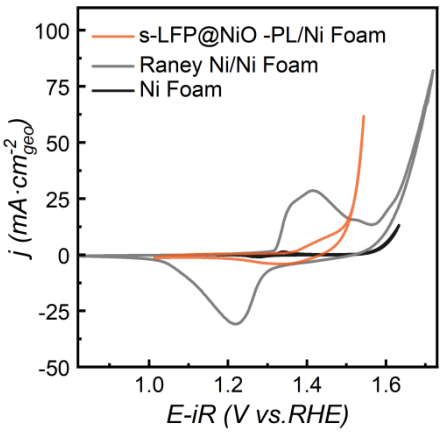

Figure S29. OER performance of the delithiated catalyst (s-LFP@NiO-PL) compared to Raney Ni. The s-LFP@NiO-PL electrode was prepared by drop-casting the catalyst ink onto Ni foam, achieving a mass loading of approximately 1.40 mg $_{(s\text{-}LFP@NiO\text{-}PL)}$·cm^{-2}. In comparison, the Raney Nickel electrode was fabricated with a significantly higher mass loading of 24 mg $_{(Raney\ Ni)}$·cm^{-2}.

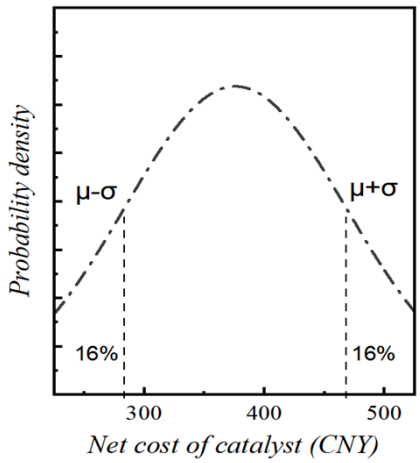

Figure S30. Probability density curve for the total cost.

Table S1. Summary of EXAFS fitting results for the s-LFP@NiO, s-LFP@NiO-OER. CN is the coordination number; R is the bond length; σ2 is the relative mean square displacement about the equilibrium path length.

Data sets	Ni-O path			Ni-Ni/Fe path		
	[a]CN_{Ni-O}	R(Å)	σ^2(Å)^2	[a]CN_{Ni-Ni}	R(Å)	σ^2(Å)^2
s-LFP@NiO	6	2.06799± 0.00533619	0.00742806± 0.000898380	12	3.04291± 0.00701241	0.01689683± 0.00098420
s-LFP@NiO-OER	6	2.06425 ± 0.00482866	0.00638442± 0.00078227	12	3.04728± 0.00584405	0.01543923± 0.00079117

[a] *Not varied in fit. The Reduced-chi-squared (χ^2) and r factor (R) for the fitting of the above 2 data sets are 85.6 and 0.0088, respectively.*

Data sets	Fe-O path		
	CN_{Fe-O}	R(Å)	σ^2(Å)^2
s-LFP@NiO	6.1488904± 0.9384155948	2.05706± 0.0094834257	0.01683867± 0.00284210
s-LFP@NiO-OER	6.83192665± 0.61799467	1.97106± 0.00719902	0.01224273± 0.00144054

The Reduced-chi-squared (χ^2) and r factor (R) for the fitting of the above 2 data sets are 84.1 and 0.0021, respectively.

Data sets	Ni-O path			Ni-Ni/Fe path			Fe-O path		
	[a]CN_{Ni-O}	R(Å)	σ^2(Å)^2	[a]CN_{Ni-Ni}	R(Å)	σ^2(Å)^2	CN_{Fe-O}	R(Å)	σ^2(Å)^2
s-LFP@NiO	6	2.06799± 0.00533619	0.00742806± 0.000898380	12	3.04291± 0.00701241	0.01689683± 0.00098420	6.1488904± 0.9384155948	2.05706± 0.0094834257	0.01683867± 0.00284210

s-LFP@NiO -OER	6	2.06425 ± 0.00482866	0.00638442± 0.00078227	12	3.04728± 0.00584405	0.01543923± 0.00079117	6.83192665± 0.61799467	1.97106± 0.00719902	0.01224273± 0.00144054

Table S2. Comparison of OER performance for the s-LFP@NiO electrocatalyst with those of various catalysts derived from spent cathode materials or other lithium-containing electrocatalysts reported in the literature

Catalyst	Synthesis method	Electrode	Mass Loading (mg cm^{-2})	Electrolyte	Overpotential (mV) @ j=10 $mAcm^{-2}$	Tafel Slope (mV dec-1)	Ref.
NCMB-2	Leachate boriding method	NF	0.3	1 M KOH	263	57.98	[31]
LNCM-G/CC	Direct recycling	CC	NA	1 M KOH	320	100.3	[32]
LNMCO-H-450S	Hydrometallurgical recycling and sulfidation	GCE	0.255	0.1 M KOH	331	118.9	[33]
Ni−Co−Mn oxides	Ball milling	GCE	0.2	1 M KOH	367	43.84	[34]
de-NCM94	Electrochemical de-lithiation	CC	10	1 M KOH	270	121	[35]
NiMnCo-AC	Hydrometallurgical recycling	GCE	0.38	1 M KOH	340	133	[36]
evolved Ni-$LiFePO_4$	Impregnation	CP	0.42	1 M KOH	285	45	[37]
$LiNi_{0.75}Fe_{0.25}PO_4$/rGO	Electrodeposition	GCE	0.04	1 M NaOH	270	47	[38]
LCO 500C	Direct recycling	GCE	0.255	0.1 M KOH	422	67.41	[39]
$MnCo_2O_4$	Hydrometallurgical recycling	CC	0.1025	1 M KOH	400	80	[40]
CoN-Gr-2	Hydrometallurgical recycling	GCE	NA	1 M KOH	280	68.83	[41]
Co_9S_8/Co_3O_4	Hydrometallurgical recycling and sulfidation	CP	1	1 M KOH	274	48.7	[42]

Ar-H_2-300 °C-DLSLCO	Chemical delithiation and heat treatment	CP	0.4	1 M KOH	361	67	[43]
CoOOH-24h	Electrochemical exfoliation	GCE	0.408	1 M KOH	301	53.8	[44]
1% La/$LiCoO_2$	Wet Chemical Precipitation	GCE	0.2	1 M KOH	330	73	[45]
$LiCoO_{1.8}Cl_{0.2}$	Hydrothermal	GCE	0.122	1 M KOH	270	55.4	[46]
30% Pt/$LiCoO_2$	Co-Precipitation	GCE	0.1	1 M KOH	285	46.8	[47]
LT-$LiCoO_2$	Hydrothermal	GCE	0.344	1 M NaOH	430	48	[48]
LCF0.2	Sol-gel	GCE	0.232	0.1 M KOH	340	50	[49]
$LiNi_{0.75}Fe_{0.25}PO_4$/rGO	Hydrothermal	GCE	0.5	1 M KOH	295	47	[50]
Fe-NiO/NiS_2	Hydrothermal	CP	NA	1 M KOH	270	40	[51]
NiFe-LDH/Fe_1-N-C	Hydrothermal	GCE	0.3	1 M KOH	290	58	[52]
Tan-CN-NiFe	Calcination	GCE	0.127	1 M KOH	320	58	[53]
s-LFP@NiO	Solvothermal	GCE	0.255	1 M KOH	269	44	
s-LFP@NiO-PL	Solvothermal and Chemical Li leaching	GCE	0.255	1 M KOH	268	38.3	This work
s-FP@NiO	Solvothermal	GCE	0.255	1 M KOH	312	75.6	

Table S3. Economic analysis for the production of 1 kg of our catalyst

	Chemicals	Mass(g)	Average Price(¥/g)	Costs (¥)
Spent LFP cost	s-LFP	796.46	0.022	17.50
Material input cost	$Ni(acac)_2$	796.46	0.53	421.48
	$K_3[Fe(CN)_6]$	1277.30	0.21	160.13
	$Na_2S_2O_8$	461.65	0.11	
	$Fe_2(SO_4)_3$	259.58	0.0985	
	H_2O_2	65.93	2.06	
	Na_2CO_3	206.40	0.073	15.07
	Total			596.68
Benefit of the Li salt produced	Li_2CO_3	143.07	1.89	270.70
Process cost	**Procedure**	**Energy consumption(kWh)**	**Price(¥/kWh)**	**Costs (¥)**
	Pretreatment	6.08	0.79	4.80
	Precipitation	1.12		0.88
	Separation	1.11		0.88
	Evaporation	0.59		0.47
	Drying	0.94		0.74
	Solvothermal	4.74		3.74
	Total	14.58	0.79	11.52

Table S4. Prices of chemicals from different purchasing sources[13, 16-30]

Chemicals	$Ni(acac)_2$	Li_2CO_3	Na_2CO_3	$K_3[Fe(CN)_6]$	$Na_2S_2O_8$	$Fe_2(SO_4)_3$
Prices from	0.33	2.20	0.092	0.19	0.12	0.072
	0.49	2.76	0.040	0.19	0.14	0.076

different purchasing sources (¥/g)	0.64	1.20	0.058	0.30	0.056	0.14
	0.49	1.44	0.092	0.25	0.086	0.096
	0.51	2.20	0.090	0.14	0.098	0.080
	0.68	2.20	0.064	0.15	0.12	0.080
	0.46	2.48	0.090	0.31	0.14	0.17
	0.68	1.44	0.048	0.15	0.12	0.080
	0.50	1.52	0.10			
	0.49	1.48	0.060			
Average price (¥/g)	0.53	1.89	0.073	0.21	0.11	0.099

Table S5 Energy consumption for the recycling of 1 kg of spent LFP batteries. (Unit: kWh)

Procedure	**Pyrometallurgical**	**Hydrometallurgical**	**Direct regeneration**	**This work**
Pretreatment	2.06	2.06	2.06	2.06
Leaching	0	0.24	0	0
Annealing	12.375	0	3.11	0
Precipitation	0	0.38	0	0.38
Separation	0.125	0.25	0	0.375
Evaporation	0	0.20	0	0.20
Drying	0.32	0.32	0	0.32
Total	14.88	3.45	5.17	3.335

The energy consumption of the pretreatment process is obtained from a reported work.[54] The estimation of energy consumption for processes other than pretreatment is based on the process conditions and the power of the corresponding devices. The process conditions for the procedures listed in Table S5 are detailed in Table S6, which are derived from several references.[55-57]The power of the corresponding devices is obtained from our laboratory and is listed in Table S7. The energy consumption of processes conducted at room temperature is considered negligible and thus ignored. For processes with temperatures higher than 100 ℃, the heating time is included in the calculations (shown in parentheses), assuming a heating rate

of 10 ℃/min. The working power is calculated by multiplying the rated power by the ratio of the working temperature/speed to the rated temperature/speed.

Table S6 Process conditions for the procedures listed in Table S5

Procedure	Pyrometallurgical	Hydrometallurgical	Direct regeneration	This work
Leaching	/	60℃，2h	/	25℃，24h
Annealing	900℃，240(+90)min	/	650℃，60(+65)min	/
Precipitation	/	95℃，2h	/	95℃，2h
Separation	8000rpm, 0.5h	8000rpm, 1h	/	8000rpm, 2h
Evaporation	0	100℃，1h	/	100℃，1h
Drying	80℃，1h	80℃，1h	/	80℃，1h

Table S7 Power of the corresponding devices

Device	Rated power	Rated temperature/speed	Procedure
Oven	400 W	200 ℃	Leaching, Precipitation, Evaporation, Drying
Tube furnace	3000 W	1200 ℃	Annealing
Centrifuge	500 W	16000 rpm	Separation
Oil bath	1000 W	300 ℃	Solvothermal

Table S8 CO_2 emission for the recycling of 1 kg of spent LFP batteries. (Unit: kg)

Procedure	Pyrometallurgical	Hydrometallurgical	Direct regeneration	This work
Pretreatment	1.10	1.10	1.10	1.10
Leaching	0	0.13	0	0

Annealing	6.64	0	1.67	0
Precipitation	0	0.20	0	0.20
Separation	0.07	0.13	0	0.20
Evaporation	0	0.11	0	0.11
Drying	0.17	0.17	0	0.17
Total	7.98	1.85	2.77	1.79

The CO_2 emission of the processes is obtained by multiplying the energy consumption to the CO_2 emission factor[15].

Table S9 Energy consumption for the production of Raney nickel and our catalyst. (Unit: kWh).

Procedure	Raney nickel	This work
Annealing: 660℃, 1 (+66) min	1.8425	/
Post heat treatment: 80℃, 180min	0.8	/
Solvothermal: 170℃, 60min+200℃, 75min	/	1.607
Total	2.6425	1.607

The process conditions for the procedures listed in Table S9 are derived from a reported work[58].

Table S10 CO_2 emission for the production of Raney nickel and our catalyst. (Unit: kg)

Procedure	Raney nickel	This work
Annealing: 660℃, 1(+60) min	0.99	/
Post heat treatment: 80℃, 180min	0.43	/
Solvothermal: 170℃, 60min+200℃, 75min	/	0.86
Total	1.42	0.86

References

1. J. Ge, X. Ren, R. R. Chen, Y. Sun, T. Wu, S. J. H. Ong and Z. J. Xu, *Angew. Chem. Int. Ed.*, 2023, **62**, e202301721.
2. J. Yu, X. Wang, M. Zhou and Q. Wang, *Energy & Environmental Science*, 2019, **12**, 2672-2677.
3. G. Kresse and J. Hafner, *Physical Review B - Condensed Matter*, 1993, **48**, 13115-13118.
4. G. F. l. Kresse, J, *Physical Review B - Condensed Matter*, 1996, **54**, 169-185.
5. K. B. John P. Perdew, and Matthias Ernzerhof, *Phys. Rev. Lett*, 1996, **77**.
6. W. Kohn and L. J. Sham, *Physical Review*, 1965, **140**, A1133-A1138.
7. S. Grimme, J. Antony, S. Ehrlich and H. Krieg, *The Journal of chemical physics*, 2010, **132**, 154104.
8. V. Wang, N. Xu, J.-C. Liu, G. Tang and W.-T. Geng, *Comput Phys Commun*, 2021, **267**, 108033.
9. K. Momma and F. Izumi, *Journal of Applied Crystallography*, 2008, **41**, 653-658.
10. G. Henkelman, B. P. Uberuaga and H. Jo?Nsson, *The Journal of Chemical Physics*, 2000, **113**, 9901-9904.
11. S. Calvin and K. E. Furst, *XAFS for everyone*, CRC Press, Boca Raton, 2013.
12. J. Zaffran, M. B. Stevens, C. D. M. Trang, M. Nagli, M. Shehadeh, S. W. Boettcher and M. Caspary Toroker, *Chem. Mater.*, 2017, **29**, 4761-4767.
13. https://www.xiyashiji.com/).
14. Y. Yongxia, M. Xiangqi, C. Hongbin, L. Xiao, L. Chenming, S. Yong, Z. Yi and S. Zhi, *Green Chemistry*, 2018, **20**, 10.1039.C1037GC03376A-.
15. https://data.ncsc.org.cn/factoryes/index.).
16. https://www.sunwaypharm.cn/).
17. https://shao-yuan.com/).
18. https://www.macklin.cn/).
19. https://www.aladdin-e.com/).
20. https://www.meryer.com/).
21. https://www.rhawn.cn/).
22. https://www.heowns.com/).
23. https://www.solarbio.com/).
24. https://www.bidepharm.com/).
25. https://www.leyan.com/).
26. https://www.energy-chemical.com/).
27. https://www.mreda.com.cn/).
28. https://www.acmec-e.com/).
29. https://www.picasso-e.com/).
30. https://karmachem.cn/).
31. Z. Chen, W. Zou, R. Zheng, W. Wei, W. Wei, B.-J. Ni and H. Chen, *Green Chemistry*, 2021, **23**, 6538-6547.
32. R. Cui, S. Wang, J. Kong, Y. Ming, T. Sun, J. Miao, Z. Lv, R. Yan and Z. Wang, *Journal of Alloys and Compounds*, 2023, **934**, 167847.
33. G. Chen, B. Yuan, J. Dang, L. Xia, C. Zhang, Q. Wang, H. Miao and J. Yuan, *Small*, 2024, **20**, 2306967.
34. F. Balqis, Y. Irmawati, D. Geng, F. A. A. Nugroho and A. Sumboja, *ACS Applied Nano Materials*, 2024, **7**, 18138-18145.

35. S. Li, X. Zhu, X. Wang, W. Luo, X. Yu, Q. Guo, K. Song, H. Tian, X. Cui and J. Shi, *Materials Chemistry Frontiers*, 2023, **7**, 5868-5878.
36. M. Jiao, Q. Zhang, C. Ye, Z. Liu, X. Zhong, J. Wang, C. Li, L. Dai, G. Zhou and H.-M. Cheng, *Proceedings of the National Academy of Sciences*, 2022, **119**, e2202202119.
37. B. Cui, C. Liu, J. Zhang, J. Lu, S. Liu, F. Chen, W. Zhou, G. Qian, Z. Wang, Y. Deng, Y. Chen and W. Hu, *Science China Materials*, 2021, **64**, 2710-2718.
38. Y. Liu, H. Wang, D. Lin, C. Liu, P.-C. Hsu, W. Liu, W. Chen and Y. Cui, *Energy & Environmental Science*, 2015, **8**, 1719-1724.
39. N. Chen, J. Qi, X. Du, Y. Wang, W. Zhang, Y. Wang, Y. Lu and S. Wang, *RSC Advances*, 2016, **6**, 103541-103545.
40. S. Natarajan, S. Anantharaj, R. J. Tayade, H. C. Bajaj and S. Kundu, *Dalton Transactions*, 2017, **46**, 14382-14392.
41. T. Liu, S. Cai, G. Zhao, Z. Gao, S. Liu, H. Li, L. Chen, M. Li, X. Yang and H. Guo, *Journal of Energy Chemistry*, 2021, **62**, 440-450.
42. H. Bian, W. Wu, Y. Zhu, C. H. Tsang, Y. Cao, J. Xu, X. Liao, Z. Lu, X.-Y. Lu, C. Liu and Z. Zhang, *ACS Sustainable Chem. Eng.*, 2023, **11**, 670-678.
43. J. Kang, D. Tang, Y. Liu, Y. Huang, W. He, Y. Liu, X. Ji, W. Li and J. Li, *Industrial & Engineering Chemistry Research*, 2023, **62**, 3882-3888.
44. C. Huang, H. Lv, Z. Yang, C. Lian, J. Du, G. Liu, W. Tang, Z. Xu, Z. Chi, H. Liu, H. Huang and W. Zhang, *Journal of Materials Chemistry A*, 2022, **10**, 3359-3372.
45. Z. Zhang, C. Liu, C. Feng, P. Gao, Y. Liu, F. Ren, Y. Zhu, C. Cao, W. Yan, R. Si, S. Zhou and J. Zeng, *Nano Letters*, 2019, **19**, 8774-8779.
46. J. Wang, S.-J. Kim, J. Liu, Y. Gao, S. Choi, J. Han, H. Shin, S. Jo, J. Kim, F. Ciucci, H. Kim, Q. Li, W. Yang, X. Long, S. Yang, S.-P. Cho, K. H. Chae, M. G. Kim, H. Kim and J. Lim, *Nature Catalysis*, 2021, **4**, 212-222.
47. X. Zheng, P. Cui, Y. Qian, G. Zhao, X. Zheng, X. Xu, Z. Cheng, Y. Liu, S. X. Dou and W. Sun, *Angew. Chem. Int. Ed.*, 2020, **59**, 14533-14540.
48. T. Maiyalagan, K. A. Jarvis, S. Therese, P. J. Ferreira and A. Manthiram, *Nature Communications*, 2014, **5**, 3949.
49. Y. Zhu, W. Zhou, Y. Chen, J. Yu, M. Liu and Z. Shao, *Adv. Mater.*, 2015, **27**, 7150-7155.
50. S. Ma, Q. Zhu, L. Chen, W. Wang and D. Chen, *Journal of Materials Chemistry A*, 2016, **4**, 8149-8154.
51. N. Zhang, Y. Hu, L. An, Q. Li, J. Yin, J. Li, R. Yang, M. Lu, S. Zhang and P. Xi, *Angewandte Chemie*, 2022, **134**, e202207217.
52. Z. Q. Liu, X. Liang, F. X. Ma, Y. X. Xiong, G. Zhang, G. Chen, L. Zhen and C. Y. Xu, *Advanced Energy Materials*, 2023, **13**, 2203609.
53. W. Wan, L. Kang, A. Schnegg, O. Ruediger, Z. Chen, C. S. Allen, L. Liu, S. Chabbra, S. DeBeer and S. Heumann, *Angewandte Chemie International Edition*, 2025, **64**, e202424629.
54. W. Wang, Z. Liu, Z. Zhu, Y. Ma, K. Zhang, Y. Meng, T. Ahmad, N. A. Khan, Q. Peng and Z. Xie, *Nature Sustainability*, 2025, **8**, 287-296.
55. B. Zhang, X. Qu, X. Chen, D. Liu, Z. Zhao, H. Xie, D. Wang and H. Yin, *Journal of Hazardous Materials*, 2022, **424**, 127586-.
56. H. Li, S. Xing, Y. Liu, F. Li, H. Guo and G. Kuan, *ACS Sustainable Chemistry & Engineering*, 2017.

57. X. Li, J. Zhang, D. Song, J. Song and L. Zhang, *Journal of Power Sources*, 2017, **345**, 78-84.
58. C. I. Bernäcker, T. Rauscher, T. Büttner, B. Kieback and L. Röntzsch, *Journal of The Electrochemical Society*, 2019, **166**, F357–F363.